Journal of Engineering Science and Technology
Vol. 18, No. 5 (2023) 2493 - 2506

FRACTURE CHARACTERISTICS OF PLA SYNTHETIC BONE SCAFFOLDS WITH DIFFERENT SPECIMEN POROSITIES

AB AZIZ BIN MOHD YUSOF[1,*], KAMARIAH MD ISA[1], MOHD AL FATIHHI MOHD SZALI[2], MAHZAN JOHAR[3], JAMALUDDIN MAHMUD[4], MUHAMAD NOOR HARUN[5]

[1]School of Mechanical Engineering, College of Engineering, Universiti Teknologi MARA, UiTM, Johor Branch, Campus Pasir Gudang, 81750, Masai, Johor
[2]Advanced Facilities Engineering Technology Research Cluster (AFET), Plant Engineering Technology (PETech) Section, Malaysian Institute of Industrial Technology, Universiti Kuala Lumpur, Malaysia
[3]Quality Engineering Research Cluster (QEREC), Quality Engineering Section, Universiti Kuala Lumpur Malaysian Institute of Industrial Technology, 81750, Masai, Johor, Malaysia
[4]School of Mechanical Engineering, College of Engineering, Universiti Teknologi MARA, 40450 Shah Alam, Selangor, Malaysia
[5]School of Mechanical Engineering, Faculty of Engineering, Universiti Teknologi Malaysia, Malaysia
*Corresponding Author: abaziz86@uitm.edu.my

Abstract

Estimation of the fracture characteristics of the bone scaffold is an important aspect to consider in designing the porous structure while complying with its biocompatibility. The basic consideration of the related items, such as the bone scaffold design, material selection, and fabrication process, is necessary to estimate the bone scaffold's characteristics accurately. This present study was conducted to investigate the effects of porosity on the synthetic bone scaffold's strength and fracture mechanics. The specimens were made from polylactic acid (PLA) using an additive manufacturing process. Five specimens with different porosities (0% to 60%) were prepared for the test. Porosity was manipulated by adjusting the pore size during the printing process. The compact tensile test was performed using a tensile testing machine at a controlled rate of 1 mm/min. Various fracture parameters were determined based on force-displacement curves. 30% porosity was found to be the highest critical stress intensity factor, K_{IC} of 0.846±0.069 MPa*$m^{1/2}$, tip opening displacement, 0.99±0.19 mm, and total fracture energy 2.12±0.34 kJ/m^2 after 0 % specimen. For each increment in the porosity, on average 53% reduction of mechanical properties happened. In conclusion, optimising printing settings and material properties with the proper pore design enhances the fracture resistance of printed bone scaffolds, which helps develop effective and reliable bone scaffold structures.

Keywords: Bone scaffold, Fracture toughness, PLA, Porosity.

1. Introduction

Synthetic bone scaffolds fabricated using 3D printing are widely used in biomedical applications to treat patients. The treatment includes replacing the original bone to regenerate the lost bone [1, 2]. The actual bone is substituted with synthetic bone, miming the cellular environment and allowing the cell to grow [1, 3]. A suitable bone scaffold design is required to promote cell growth by providing cell mobility and nutrition flow. The synthetic bone scaffold is fabricated with a highly cross-linked network that includes complex porosity geometries [3, 5]. The bone is expected to work under the applied load by providing good load dissipation, which matches the replaced tissues [1]. However, the bone loses its strength and fractures under specific working conditions. This failure impairs the functionality of the bone scaffold and inhibits cell growth in the affected area.

Fracture mechanics combine the mechanism of the cracking body and the material properties. Cracks have a high tendency to occur in the working environment of the bone scaffold [6]. This is attributed to the design flaw or material properties of the component. Understanding the fracture behaviour of the bone scaffold requires establishing its fracture mechanics and structural response besides the material properties [7-9]. Fractures begin when the flaw in the component becomes unstable, causing the rupture. Energy dissipation of the loaded structure contributes to the fracture, where the rate of the potential energy release at the crack area can be used to determine the fracture. The fracture may occur abruptly, owing to the presence of the stress concentration and the crack's ability to traverse across the structure.

The effect of the porosity on the bone scaffold is a crucial element which can extend the component life service besides to fulfil its function [8, 10]. The bone scaffolds are subjected to continuous cycling mechanical loading, which tests the durability and workability of the structure [11]. These aspects influence its integrity and reliability as a substitute for the missing bone. The standard stress-strain test method does not allow for analysing the involved bone scaffold failure and failure mode [12]. Instead, the compact tension fracture test is preferred. The test applies two equal forces in opposite directions by introducing a notch to initiate a crack in the specimens [8, 13, 14]. Linear elastic fracture toughness and stress intensity are obtained through the test by propagating cracks caused by stress intensity.

Several studies have been found to work on the fracture of the bone scaffold. Milan et al. [15] investigated the scaffold failure mode. The study highlighted the highest stress indicated on the thin pore wall that causes structural failure. Besides, the bone scaffold deforms due to buckling under the applied load. To improve fracture toughness and reliability, Roohani-Esfahani et al. [16] introduced a unique microstructural design that aims to approach the mechanical properties of the actual bone. The unique microstructural was expected to suit the load-bearing condition. Microcracking caused by the fracture is a critical issue that must be addressed. The fracture toughness of the human bone must be considered, and this study was carried out by Norman et al. [14]. The study calculates a fracture toughness value based on the stress intensity factor and energy release. The range of crack growth, bone thickness, and material assumptions for applying linear elastic fracture affect the fracture toughness in human bone.

Study on the fracture of the bone scaffold has important applications in the bone scaffold, especially related to the 3D printing process. Farid Triawan explored the

printing parameters' influence on fracture behaviour under the tensile load [17]. By changing the amount of PLA incorporated into the tested specimen, Young's modulus and strength also increase as it relates to density. Difference design of the printed scaffold shows different mechanical properties, as the study by Ariffin et al. [9]. It is found that the circular-shaped pore is better than square-shaped pores under compression stress, which affects its fracture. This mechanical aspect influences its application, such as implant and bone replacement, by providing structural support. The fracture characteristics of bone scaffolds directly affect bone tissue engineering and implant design. The fracture can happen either under tension or compression. Arumugam reported compressive stress of the tested scaffold is double (380 ± 7.12 MPa) the tensile stress (120 ± 1.09 MPa) [18]. Thus, better consideration is required to balance the mechanical properties, durability, and unique pore structure.

As mentioned previously, the mechanical properties of bone scaffolds, especially fracture characteristics under tensile, are not much explored. The strength of the scaffold under tensile is much lower than the compression. Thus, the reliability and characteristics of the loaded structure under tensile are critical to be considered. The study aims to investigate the effects of porosity on the synthetic bone scaffold's strength and fracture mechanics. The experiment used a compact disk-shaped test, with five specimens tested based on the percentage of the structure's porosity. The specimens were fabricated using 3D printing [4, 19, 20]. The current study focused on the basic circular pore of the bone scaffold [19, 21].

2.Method

Specimens were prepared using a 3D printer (Ender-3 V2 3D Printer, Creality), where they were designed following the ASTM standard E1820. The disk-shaped specimen was chosen to determine the fracture mechanics because it was simple to prepare using a 3D printing process, cost-effective, flexible, and reliable in the test outcome. The specimens were produced layer-by-layer, with the computer controlling the process, which transformed the 3D STL file into physical 3D bone scaffold parts. Five specimen models were chosen for the study, ranging from 0% to 60% of the porosity. The porosity was varied by manipulating the pore size. The specimen's porosity strength and fracture characteristics can be appropriately obtained using different structures. All the specimens had a circular cross-section with a notch at their centre. Figure 1 depicts the model's specifications and dimensions.

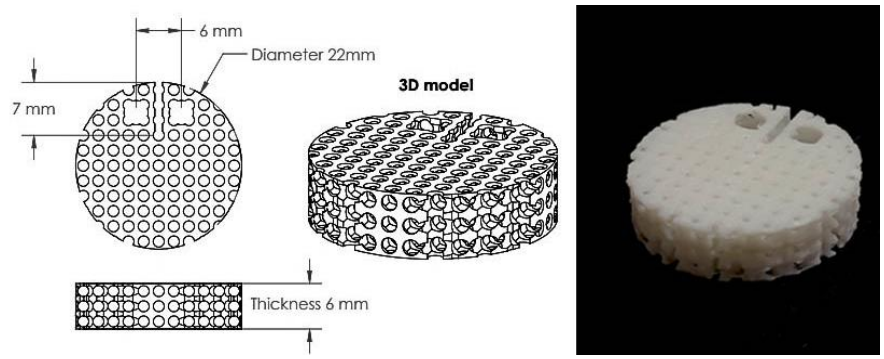

Fig. 1. Specimen geometry and dimension.

Specimens of the bone scaffold were printed using Polylactic acid (PLA), a thermoplastic monomer with good biodegradable material characteristics. The material was suitable for medical applications and widely used in tissue engineering [4, 22]. The material was printed using specific controlled parameters, as in Table 1. These printing parameters were applied to all models to ensure the specimen's consistency.

Table 1. Printing condition.

Printing parameter	Detail value
Printing temperature	210°C
Nozzle size	0.4mm
Bed temperature	60°C
Layer width	0.4mm
Layer height	0.2mm
Infill percentage	100%
Infill speed	80 mm/s
Filament diameter	1.75mm
Printing speed	80 mm/s

The narrow notch of the notch stater configuration is introduced at the centre of the specimen during the design process to simulate the crack formation during the tensile test [13]. Both the specimen's left and right sides are symmetrical to ensure the design's effect is minimal and the stress is localised at the centre closest to the notch area.

Testing compact tensile test

Fractures occur as a result of a flaw in the bone scaffold. The fracture modes were categorized as Mode 1, Mode 2, and Mode 3. Mode 1 was preferred in this study, where the load was applied perpendicular to the crack direction [23]. Tensile forces cause the crack to move directly apart [24]. The tested specimen received no shear traction or shear displacement.

The compact tensile test was performed using a tensile testing machine (Shimadzu, AGX-V Series, North America). The specimens were clamped on the custom-made jig, as shown in Fig. 2. The testing was carried out based on the ASTM standard E1820. The standard provides guidelines for conducting tensile tests on metallic and non-metallic materials, including plastics like PLA by Jia and Wong [25], McClintock [26], and Aliheidari et al. [27]. The test was conducted at a control running mode rate of 1 mm/min. Most specimens failed at a range of 2 mm to 3 mm of distance travelled when high strain rate conditions were achieved. Force displacement curves were recorded to determine the critical load, fracture toughness (K), critical stress intensity factor (K_{IC}), tip opening displacement, total fracture energy (G_F), and plastic energy observed based on the area under the graph of the force-displacement curve [28].

The test focused on the bone scaffold's ability to prevent fracture and propagation of the notch's pre-existing crack. Different specimens are expected to have distinct fracture toughness values. Generally, the experiment was repeated until all specimens, 0% to 60% porosity, were tested. The average and standard deviation of all specimens were calculated.

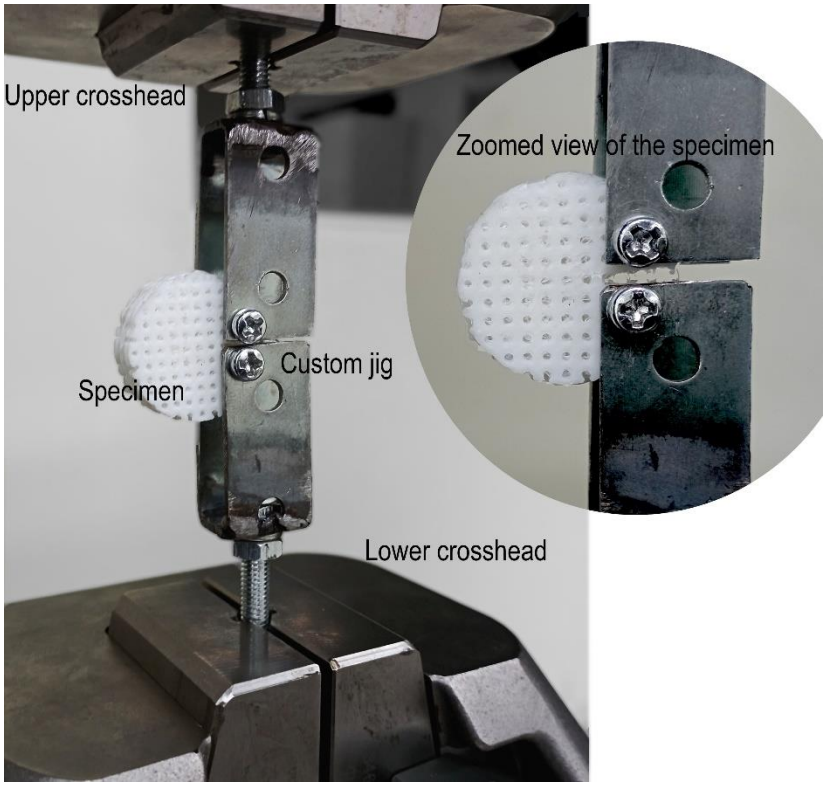

Fig. 2. Experimental setup.

The critical loading was captured based on the extrapolation of the 95% secant line from the original slope of the load-displacement curve. The intersection between the secant line and load-displacement curve was used to determine the critical load experienced by the specimens [29]. The average ratio for the P_{max}/P_Q was 1.06, which is less than 1.10. Thus, the stress intensity factor K_Q can be calculated using the following equation: In the case of P_{max}/P_Q over 1.10, the calculated K_Q possibly has no relation to K_{IC} [30]. The stress intensity factor for the bone scaffold for compact disc-shaped specimens equals [23, 31]. The detail of the equation can be referred to [13].

$$K_Q = \frac{P_Q}{\sqrt{B^2 W}} f\left(\frac{a_0}{W}\right) \quad (1)$$

where

$$f\left(\frac{a_0}{W}\right) = \frac{\left(2+\frac{a}{w}\right)}{\left(1-\frac{a}{w}\right)^{3/2}} \left[0.76 + 4.8\left(\frac{a}{w}\right) - 11.58\left(\frac{a}{w}\right)^2 + 11.43\left(\frac{a}{w}\right)^3 - 4.08\left(\frac{a}{w}\right)^4 + 4.951\left(\frac{a}{w}\right)^5\right] \quad (2)$$

where B is the thickness of the bone scaffold specimen, and W is the length from the bottom of the specimen to the centre of the fixed hole, while a_0 is the length of the initial crack from the centre of the fixed hole to the tip notch.

Fracture energy (G_f) is the work done for performing fractures (W_f) on the bone scaffold per fracture zone area. The work done is represented by the area under the load-displacement graphs. The fracture zone area was calculated using the specimen's thickness multiplied by the diameter of the specimen (D), minus the length of the notch (n). The detail of the equation can be referred to [32].

$$G_f = \frac{W_f}{A_f} \tag{3}$$

where $A_f = D - n$

3. Result

Characteristics of the tested specimens under the applied load are shown in Fig. 3.. The force-displacement curve of all five-bone scaffolds is represented in the graph. The graph is divided into three sections: pre-peak, peak, and post-peak. In the first part, pre-peak, the curve behaved linearly, and increasing displacement directly affected the load. The load approached the proximity of the peak micro-crack, localised around the notch area. The specimen started to act plastically, and irreversible deformation occurred. Rapid crack propagation occurred during the post-peak, separating the specimen at the disc's centre in half. As cracks increased further during post-peak, the durability of the specimens degraded; thus, the load decreased gradually with an increment in the displacement until the structure separated in half.

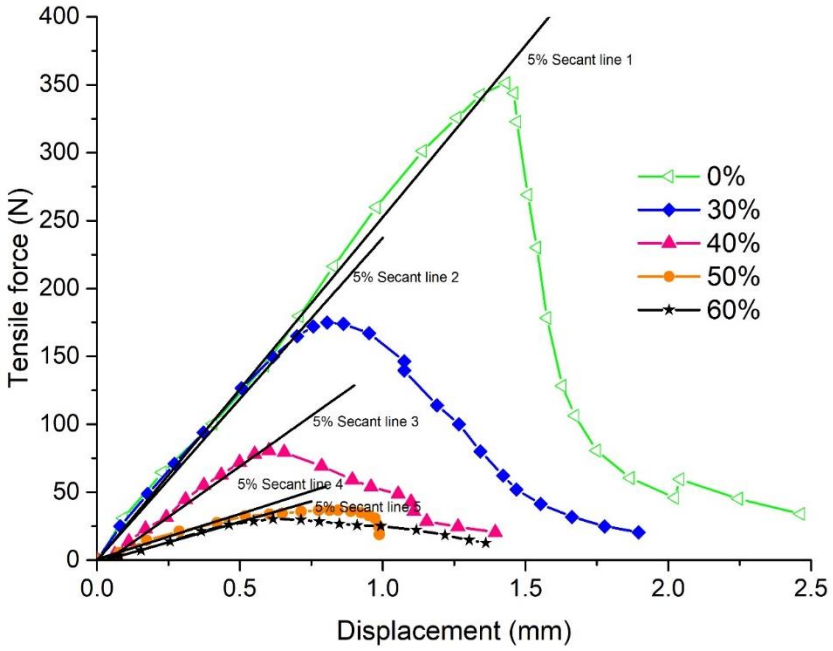

Fig. 3. Load displacement curve.

A 5% secant line was used to determine the bone scaffold characteristics for the test (Mode I). The intersection point between the secant line for each bone scaffold

porosity represents the force P_Q. The force value was collected at the intersection between the load-displacement graph and the 5% secant line when the intersection point was lower than $P_{max,}$ and the ratio of P_{max}/P_Q was not more than 1.10 [13, 29, 31]. The value of the P_Q is shown in Table 2. P_Q reduces exponentially by about 50% for a 10% increment of porosity, and the reduction of P_Q stops as it reaches 50–60% porosity.

Table 2. Experimental result for the bone scaffold specimen.

Specimen	P_Q (N)	G_f (kJ/m^2)	K_{IC} (MPa*m$^{1/2}$)	Displacement at max load (mm)
0%	317±53.3	4.14±0.15	1.595±0.268	1.41±0.12
30%	168±13.8	2.12±0.34	0.846±0.069	0.99±0.19
40%	80±7.6	0.72±0.02	0.400±0.039	0.59±0.06
50%	33.9±0.7	0.25±0.072	0.170±0.004	0.65±0.14
60%	26.8±4.3	0.40±0.080	0.135±0.022	1.0±0.37

Figure 3 and Table 2 show that the compact tensile test ranked the specimens according to their fracture behaviour. The rank's characteristics are based on the P_Q and K_{IC} loads. The highest P_Q is a solid specimen with 0% porosity. Introducing 30% porosity to the sample caused a reduction of the P_Q load by 47% to 168±13.8 N. 40% of the porosity was introduced to the 4th specimen, causing a 53% reduction in the P_Q load to 80±7.6 N. A further reduction occurred for the 50% porosity specimen, which reduced the P_Q load by 57% to 33.9±0.7 N. Finally, the 60% porosity specimen reduced the P_Q load by 20 % to 26.8±4.3 N. This rank represents the bone scaffold's response capability under the applied load. Even though the structure's porosity is important to cell growth, it must not compromise the strength of the structure toward fracture.

The maximum load of the load-displacement curve is shown in Fig. 4. Five specimens were tested for each of the porosity. Averages and standard deviations were calculated from the experimental data. All specimens had higher repeatability and reproducibility with a lower average standard deviation of 8.9%. Generally, the maximum load P_{max} followed the same pattern as the load $P_{Q.}$ Increasing porosity decreased the load. As expected, increasing the porosity of the specimen caused P_{max} to reduce as the bone scaffold's column size became smaller. The reduction for the 30% porosity specimen was more significant than for the 0% porosity or solid sample. Further increasing the porosity by 10% caused a decrease in P_{max} by half of the previous bone scaffold strength. However, it was observed that after a 50% reduction of porosity, further reduction of the porosity did not significantly affect Pmax, probably due to the brittleness of the porous structure.

Figure 5 shows the crack propagation of the bone scaffold at the post-peak deformation. As the displacement increased from 1.41 mm to 0.59 mm, as shown in Table 2, the tensile stress was localised and concentrated at the notch tip. This concentrated stress area became a flaw in the bone scaffold structure, which would later become unstable and lead to fracture. The structural failure occurred on the vertical column at 90 degrees to the crack propagation direction. Introducing the higher porosity reduced the crack resistance, especially in the higher porosity structure. In Fig. 5(c), even though the applied displacement is less compared to those of Fig. 5(a) and 5(b), the structure failed, fully separating into two parts;

eventually, the crack was initiated at the lower load. As applied displacement keeps increasing, strain energy acting on the bone scaffold increases, resulting in the rapid growth of the crack as the magnitude of the strain energy is higher than the surface energy of the PLA.

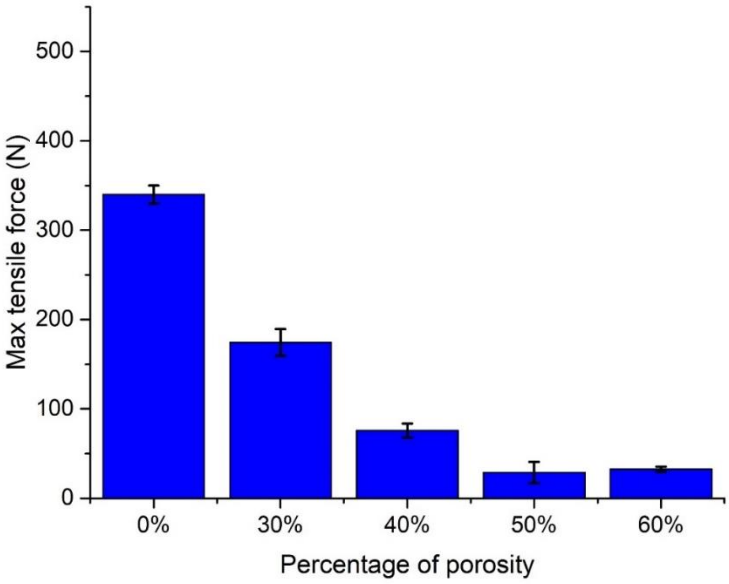

Fig. 4. Facture energy and maximum tensile force.

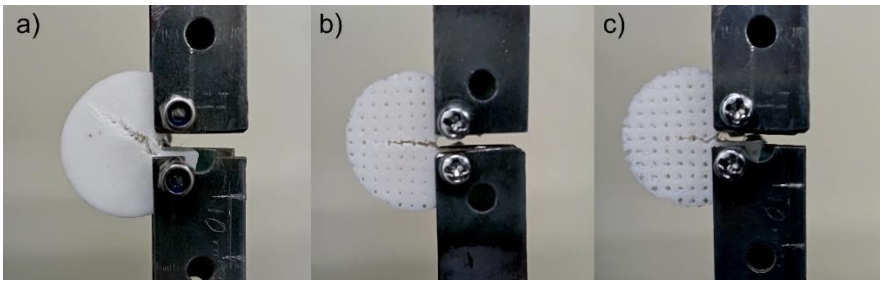

Fig. 5. Fracture mode (a) Solid specimen (b) Specimen with 30% porosity (c) Specimen with 50% Porosity.

4. Discussion

As mentioned in Section 3, the load-displacement curve is divided into three stages: 1) the pre-peak stage, 2) the peak stage, and 3) the post-peak stage. The 0% porosity specimen showed the highest increment rate, which reduced gradually as porosity increased due to the reduction of structural stiffness. Besides the presence of porosity in the bone scaffold, the linear elasticity of the bone scaffold was lower than that of the reported Young's modulus, as the 3D printing process and its structure affected the internal interaction between the PLA layer. At the peak stage, microcracks damaged the specimen's structure close to the notch tip. The crack propagated progressively perpendicular to the loading direction for Mode 1,

degrading the specimen's structural strength. The crack was further propagated in the post-peak stage as the displacement increased. Similar to the increment rate of the pre-peak stage, the reduction rate also decreases as porosity increases.

The critical stress intensity factor is an important mechanical property that characterises PLA's resistance to crack propagation and fracture toward the applied load. For the experimental validation purpose, the K_{IC} value of the 0% specimen agrees with the previous studies, which ranged from 0.7 to 2.0 MPa*m1/2 [33, 34]. The variation of the result depends on factors such as the specific grade of PLA, its molecular weight, processing conditions, and testing methods [33, 35].

The crack propagation was related to printing orientation and the load direction (Mode 1). Specimens with porosity (30% to 60%) experienced cracks propagation perpendicular to the loading direction. The trend was related to the column of the porosity being pulled on tension along its length, thus experiencing higher tensile stress. To balance the applied tensile, the column of the bone scaffold reacted by balancing the load and generating internal stress. When the stress increased, causing the crack initiation at the notch tip and propagating further. However, specimen with 0% porosity showed a 45-degree orientation in the crack propagation trend, following printing orientation with a small abrupt that altered propagation direction. Besides, the critical displacement separation generally increases with porosity, as in Fig. 3, and the crack growth rate in the affected region is faster with increasing porosity.

The circular nozzle used to fabricate the specimens using 3D printing introduced a higher inter-bead void between the printed layers. Altering the porosity caused the percentage of the inter-bead void to increase and eventually reduce the inter-layer bonding strength. The inter-bead void causes higher stress concentration under a high-stress state, especially in the crack-tip area. The declining value was observed in $P_{max,}$ with decreased exponentially with porosity. Consequently, lower the fracture energy as in Table 2. Inter-bead fusion was an essential characteristic of producing a good sample during printing. Specimen porosity varied by increasing the pore size and reducing the wall thickness, causing inter-bead fusion during the printing process to become challenging. Besides, the porosity also increased the brittleness and reduced the ductility of the specimen. Generally, all the specimens were printed with a 45° orientation, which contributed to the resilience of the bonding and increased the fracture resistance. Typically, the load orientation alters based on the bone scaffold's microstructure [23]. However, in some cases, 90° printing orientation is preferred as the bead layer is loaded along its length and introduces higher resistance to fracture. Even though the print was focused at 45°, under the tensile, the printing orientation did not significantly influence crack propagation since the higher stress was experienced at the middle wall column.

Experimental testing indicates that the critical stress intensity factor for the fracture criterion varied with the percentage of porosity. Two district groups can be distinguished from the experimental data, depending on the thickness of the wall columns, either thick or thin. In addition, the column size depends on the pore size; the bigger the porosity, the smaller the column size. The load-displacement curve, as in Fig. 3, can be used to explain the fracture mechanics of both regions. Group 1 corresponds to the thick wall column for the lower per cent of porosity. The load-displacement responds linearly, with a faster increment in its gradient. For group 2,

the thin-walled column, the load-displacement responded less with a lower graph's gradient. At this point, 50% and 60% porosity indicated almost the same value. It was discovered that to print 50% dan 60% specimens, the fabrication process becomes challenging due to the printing resolution, also known as layer height in Z height. Due to the printing limitation, the printed specimens showed almost similar brittleness properties. Besides that, both specimens also failed rapidly due to lower crack resistance and unstable crack propagation.

For higher bone scaffold porosities, progressive damages on the adjacent wall were observed, representing the brittle fracture behaviour of the specimen. Both values of maximum load (P_{max}) and fracture energy (G_f) showed a similar pattern of magnitude reduction. A qualitative investigation of the higher porosity reveals that higher de-bonding of the inter-bead layer significantly reduced structural strength. The de-bonding between inter-bead layers can be reduced by introducing or optimising the printing settings, such as printing speed, bed, and printing temperature, with a proper cooling cycle. Higher porosity absorbs less energy than lower porosity due to the density of the structure. Lower porosity contains more PLA material, which increases the bone scaffold's ductility to absorb more energy during the test up to the fracture, causing a strong effect on fracture behaviour.

Synthetic bone scaffolds can be engineered to mimic certain aspects of bone's mechanical properties, especially the cancellous bone structure. The fracture toughness of synthetic bone scaffolds could be modified to behave similarly to actual bone using proper material properties and microstructure. Based on the previous study, cancellous bone's Critical stress intensity factor ranged from 0.08 MPa*m1/2 to 0.70 MPa*m1/2 depending on the bone density [36, 37]. These values agree with the current result, ranging from 0.135±0.022 MPa*m1/2 to 0.846±0.069 MPa*m1/2 for different porosity values. Even though the current result matches the actual bone, better consideration is required to ensure the synthetic bone scaffolds can fully replicate the natural composite material of fibers embedded in a mineral matrix to provide excellent fracture toughness and strength.

5. Conclusions

The study revealed that porosity significantly influences the fracture characteristics and mechanical properties of 3D-printed bone scaffold specimens. As the porosity increased, the specimens exhibited a gradual reduction of P_{max} from 340N ± 9.9N to 32N ± 2.8N, fracture toughness from 1.595MPa*$m^{1/2}$ ± 0.268MPa*$m^{1/2}$ to 0.135MPa*$m^{1/2}$ ± 0.022MPa*$m^{1/2}$ and fracture energy 4.14kJ/m^2 ± 0.15kJ/m^2 to 0.40kJ/m^2 ± 0.080kJ/m^2. Higher porosity resulted in more brittle fracture behaviour due to increased inter-bead voids and reduced inter-layer bonding strength. Furthermore, the lower bone scaffold porosity encourages cell growth by providing a suitable environment that matches structural reliability. It is important to balance the porosity for cell growth without compromising the structural integrity and resistance to fracture. The study has provided valuable insights for developing effective and reliable bone scaffold structures directly affecting bone tissue engineering.

Acknowledgement

This study was supported by Universiti Teknologi MARA, UiTM, under Grant Penyelidikan MyRA (600-RMC/GPM LPHD 5/3 (110/2021)).

Nomenclatures

A_f	Fracture zone area, m^2
a_0	Length of the initial crack, m
B	Thickness of the bone scaffold specimen, m
D	Diameter of the specimen, m
G_f	Fracture energy, kJ/m^2
K_{IC}	Critical stress intensity factor, $MPa*m^{1/2}$
K_Q	Stress intensity factor, $MPa*m^{1/2}$
n	Length of the notch, m
P_Q	Intersection points between the secant line and force-displacement curve, N
P_{max}	Maximum force, N
W	Length from the bottom of the specimen, m
W_f	Work done for performing fractures, Nm

Abbreviations

3D	Three dimensional
PLA	Polylactic acid
STL	Standard Tessellation Language

References

1. Gregor, A.; Filová, E.,; Novák, M.; Kronek, J.; Chlup, H.; Buzgo, M.; Blahnová, V.; Lukášová, V.; Bartoš, M.; Nečas, A.; and Hošek, J. (2017). Designing of PLA scaffolds for bone tissue replacement fabricated by ordinary commercial 3D printer. *Journal of Biological Engineering*, 11(1), 1-21.
2. Martin, V.; Ribeiro, I. A.; Alves, M.M.; Gonçalves, L.; Claudio, R.A.; Grenho, L.; Fernandes M.H; Gomes, P.; Santos, C.F; and Bettencourt, A.F. (2019). Engineering a multifunctional 3D-printed PLA-collagen-minocycline-nanoHydroxyapatite scaffold with combined antimicrobial and osteogenic effects for bone regeneration. *Materials Science and Engineering: C*, 101, 15-26.
3. Kao, C.T.; Lin, C.C.; Chen, Y.W.; Yeh, C.H.; Fang, H.Y.; and Shie, M.Y. (2015). Poly(dopamine) coating of 3D printed poly(lactic acid) scaffolds for bone tissue engineering. *Materials Science and Engineering: C*, 56, 165-173.
4. Vazquez-Vazquez, F.C.; Chanes-Cuevas, O.A.; Masuoka, D.; Alatorre, J.A.; Chavarria-Bolaños, D.; Vega-Baudrit, J.R.; Serrano-Bello, J.; and Alvarez-Perez, M.A. (2019). Biocompatibility of developing 3D-printed tubular scaffold coated with nanofibers for bone applications. *Journal of Nanomaterials*, 2019, Article 6105818.
5. Kusumastuti, Y.; Kobayashi, M.; Purwaningtyas, F.Y.; Najmina, M.; Petrus, H.T.B.M.; Eviana, N.R.; Budhijanto; and Tanihara, M. (2018). Characterization of three dimensional scaffolds from local chitosan/alginate/geothermal silica for potential tissue engineering applications. *Journal of Engineering Science and Technology*, 13(11), 3500-3506.
6. Entezari, A.; Roohani-Esfahani, S.I.; Zhang, Z.; Zreiqat, H.; Dunstan, C.R.; and Li, Q. (2016). Fracture behaviors of ceramic tissue scaffolds for load bearing applications. *Scientific Reports*, 6(1), 28816.

7. Fu, Q.; Saiz, E.; Rahaman, M.N. ; and Tomsia, A.P. (2013). Toward strong and tough glass and ceramic scaffolds for bone repair. *Advanced Functional Materials*, 23(44), 5461-5476.
8. Carlsson, J.; Braesch-Andersen, A.; Ferguson, S. J.; and Isaksson, P. (2023). Fracture in porous bone analysed with a numerical phase-field dynamical model. *Journal of the Mechanical Behavior of Biomedical Materials*, 139, 105659.
9. Ariffin, M.K.A.M.; Fazel, S.H.; Ismail, M.I.S.; Mohamed, S.B.; and Wahid, Z. (2018). Mechanical properties of bone scaffold prototypes fabricated by 3D printer. *Journal of Engineering Science and Technology*, Special Issue 12/2018, 29-38.
10. Patel, P.P.; Buckley, C.; Taylor, B. L.; Sahyoun, C.C.; Patel, S.D.; Mont, A.J.; Mai, L.; Patel, S.; and Freeman, J. W. (2019). Mechanical and biological evaluation of a hydroxyapatite-reinforced scaffold for bone regeneration. *Journal of Biomedical Materials Research Part A*, 107(4), 732-741.
11. Shuai, C.; Peng, B.; Feng, P.; Yu, L.; Lai, R.; and Min, A. (2022). In situ synthesis of hydroxyapatite nanorods on graphene oxide nanosheets and their reinforcement in biopolymer scaffold. *Journal of Advanced Research*, 35, 13-24.
12. Kim, H.-W.; Knowles, J.C.; and Kim, H.-E. (2004). Development of hydroxyapatite bone scaffold for controlled drug release via poly (ϵ - caprolactone) and hydroxyapatite hybrid coatings. *Journal of Biomedical Materials Research Part B: Applied Biomaterials*, 70(2), 240-249.
13. Astm, E. (1820). Standard test method for measurement of fracture toughness. *ASTM, Annual Book of Standards*, 3.
14. Norman, T.L.; Vashishth, D.; and Burr, D. B. (1995). Fracture toughness of human bone under tension. *Journal of Biomechanics*, 28(3), 309-320.
15. Milan, J.-L.; Sandino, C.; Midderhoff, S.; Marques, L.; Planell, J.A.; and Lacroix, D. (2009). Mode of failure of a biomaterial composite scaffold for bone tissue engineering using synchrotron micro-tomography and finite element analysis. *Proceedings of the* 12*th International Conference on Fracture (ICF)*, Ottawa, Canada, 1-8.
16. Roohani-Esfahani, S.I.; Dunstan, C.R.; Li, J.J.; Lu, Z.; Davies, B.; Pearce, S.; Field, J.; Williams, R.; and Zreiqat, H. (2013). Unique microstructural design of ceramic scaffolds for bone regeneration under load. *Acta Biomaterialia*, 9(6), 7014-7024.
17. Triawan, F.; Syefira, D.; Rismalia, M.; Suryani, I.O.; Djamari, D.W.; Budiman, B.A.; and Nandiyanto, A.B.D. (2022). The influence on infill density and pattern on the mechanical and fracture behavior of 3D printed structure subject to uniaxial tensile load. *Journal of Engineering Science and Technology*, 17(5), 3254-3266.
18. Arumugam, S.; Kandasamy, J.; Md Shah, A.U.; Hameed Sultan, M.T.; Safri, S.N.A.; Abdul Majid, M.S.; Basri, A.A.; and Mustapha, F. (2020). Investigations on the mechanical properties of glass fiber/sisal fiber/chitosan reinforced hybrid polymer sandwich composite scaffolds for bone fracture fixation applications. *Polymers*, 12(7), 1501.
19. Deng, F.; Liu, L.; Li, Z.; and Liu, J. (2021). 3D printed Ti6Al4V bone scaffolds with different pore structure effects on bone ingrowth. *Journal of Biological Engineering*, 15(1), 4.

20. Gregor, A.; Filová, E.; Novák, M.; Kronek, J.; Chlup, H.; Buzgo, M.; Blahnová, V.; Lukášová, V.; Bartoš, M.; Nečas, A.; and Hošek, J. (2017). Designing of PLA scaffolds for bone tissue replacement fabricated by ordinary commercial 3D printer. *Journal of Biological Engineering*, 11(1), 31.
21. Yusof, A.A.M.; Januddi, M.A.M.S.; Isa, K.M.; Khalid, M.F.S.; and Abdul Kadir, R.A. (2022). The effect of porosity and contact angle on the fluid capillary rise for bone scaffold wettability and absorption. *Malaysian Journal of Medicine and Health*, 18(SUPP6), 6-11.
22. Mohammadi-Zerankeshi, M.; and Alizadeh, R. (2023). 3D-printed PLA-Gr-Mg composite scaffolds for bone tissue engineering applications. *Journal of Materials Research and Technology*, 22, 2440-2446.
23. Papon, E.A.; and Haque, A. (2019). Fracture toughness of additively manufactured carbon fiber reinforced composites. *Additive Manufacturing*, 26, 41-52.
24. Huo, P.; Zhao, Z.; Bai, P.; Yuan, X.; Wang, Q.; Zhao, R.; Zhang, L.; Du, W.; Han, B.; and Wang, Y. (2021). Deformation evolution and fracture mechanism of porous TC4 alloy scaffolds fabricated using selective laser melting under uniaxial compression. *Journal of Alloys and Compounds*, 861, 158529.
25. Jia, Z.; and Wang, L. (2019). 3D printing of biomimetic composites with improved fracture toughness. *Acta Materialia*, 173, 61-73.
26. McClintock, F.A.; and Irwin, G.R. (1968). *Plasticity aspects of fracture*. In Liebowitz, H. *Fracture: An Advanced Treatise*.Academic Press.
27. Aliheidari, N.; Tripuraneni, R.; Ameli, A.; and Nadimpalli, S. (2017). Fracture resistance measurement of fused deposition modeling 3D printed polymers. *Polymer Testing*, 60, 94-101.
28. Srinivasan, M.; and Seetharamu, S. (2012). Fracture toughness of metal castings. *Science and Technology of Casting Processes*, 285-312.
29. Lemesle, J.; Hubert, C.; and Bigerelle, M. (2020). Numerical study of the toughness of complex metal matrix composite topologies. *Applied Sciences*, 10(18), 6250.
30. Ben Jar, P.Y.; and Adianto, R. (1967). Determination of plane strain fracture toughness. *Materials Research and Standards*, 7(6), 262-266.
31. Hertzberg, R.W.; Vinci, R.P.; and Hertzberg, J.L. (2012). Deformation and fracture mechanics of engineering materials (5^{th} ed.), Wiley.
32. Yang, J.; Lian, H.; Liang, W.; Nguyen, V.P.; and Bordas, S.P. (2019). Model I cohesive zone models of different rank coals. *International Journal of Rock Mechanics and Mining Sciences*, 115, 145-156.
33. Cem, B.O.Ğ.A.; and Seyedzavvar, M. (2021). A study on the effects of the interior architecture on the fracture toughness of 3D printed PLA samples. *Avrupa Bilim ve Teknoloji Dergisi*, (32), 14-19.
34. 34. Chen, J.; Zhang, T.Y.; Jin, F.L.; and Park, S.J. (2018). Fracture toughness improvement of poly (lactic acid) reinforced with poly (ε-caprolactone) and surface-modified silicon carbide. *Advances in Materials Science and Engineering*, 2018, Article ID 6537621.

35. Todo, M.; and Takayama, T. (2011). Fracture mechanisms of biodegradable PLA and PLA/PCL blends. In Pignatello, R. *Biomaterials-Physics and Chemistry*. IntechOpen.
36. Greenwood, C.; Clement, J.G.; Dicken, A.J.; Evans, J.P.O.; Lyburn, I.D.; Martin, R.M.; Rogers, K.D.; Stone, N.; Adams, G.; and Zioupos, P. (2015). The micro-architecture of human cancellous bone from fracture neck of femur patients in relation to the structural integrity and fracture toughness of the tissue. *Bone Reports*, 3, 67-75.
37. Cook, R.B.; Curwen, C.; Tasker, T.; and Zioupos, P. (2010). Fracture toughness and compressive properties of cancellous bone at the head of the femur and relationships to non-invasive skeletal assessment measurements. *Medical Engineering & Physics*, 32(9), 991-997.